nanomaterials

MDPI

Article

Elucidation of the Crystal Growth Characteristics of SnO_2 Nanoaggregates Formed by Sequential Low-Temperature Sol-Gel Reaction and Freeze Drying

Saeid Vafaei [1,*], Alexander Wolosz [1], Catlin Ethridge [1], Udo Schnupf [2], Nagisa Hattori [3], Takashi Sugiura [3] and Kazuhiro Manseki [3,*]

[1] Mechanical Engineering Department, Bradley University, 1501 West Bradley Avenue, Peoria, IL 61625, USA; awolosz@mail.bradley.edu (A.W.); cethridge@mail.bradley.edu (C.E.)
[2] Mund-Lagowski Department of Chemistry and Biochemistry, Bradley University, 1501 West Bradley Avenue, Peoria, IL 61625, USA; uschnupf@fsmail.bradley.edu
[3] Graduate School of Natural Science and Technology, Gifu University, Gifu 501-1193, Japan; a4524054@edu.gifu-u.ac.jp (N.H.); tsugiura@gifu-u.ac.jp (T.S.)
* Correspondence: svafaei@fsmail.bradley.edu (S.V.); kmanseki@gifu-u.ac.jp (K.M.)

Abstract: SnO_2 nanoparticles are regarded as attractive, functional materials because of their versatile applications. SnO_2 nanoaggregates with single-nanometer-scale lumpy surfaces provide opportunities to enhance hetero-material interfacial areas, leading to the performance improvement of materials and devices. For the first time, we demonstrate that SnO_2 nanoaggregates with oxygen vacancies can be produced by a simple, low-temperature sol-gel approach combined with freeze-drying. We characterize the initiation of the low-temperature crystal growth of the obtained SnO_2 nanoaggregates using high-resolution transmission electron microscopy (HRTEM). The results indicate that Sn (II) hydroxide precursors are converted into submicrometer-scale nanoaggregates consisting of uniform SnO_2 spherical nanocrystals (2~5 nm in size). As the sol-gel reaction time increases, further crystallization is observed through the neighboring particles in a confined part of the aggregates, while the specific surface areas of the SnO_2 samples increase concomitantly. In addition, X-ray photoelectron spectroscopy (XPS) measurements suggest that Sn (II) ions exist in the SnO_2 samples when the reactions are stopped after a short time or when a relatively high concentration of Sn (II) is involved in the corresponding sol-gel reactions. Understanding this low-temperature growth of 3D SnO_2 will provide new avenues for developing and producing high-performance, photofunctional nanomaterials via a cost-effective and scalable method.

Keywords: nanoparticles; SnO_2; crystallization; freeze drying; low-temperature synthesis; oxygen vacancies

check for updates

Citation: Vafaei, S.; Wolosz, A.; Ethridge, C.; Schnupf, U.; Hattori, N.; Sugiura, T.; Manseki, K. Elucidation of the Crystal Growth Characteristics of SnO_2 Nanoaggregates Formed by Sequential Low-Temperature Sol-Gel Reaction and Freeze Drying. *Nanomaterials* **2021**, *11*, 1738. https://doi.org/10.3390/nano11071738

Academic Editor: David Maria Tobaldi

Received: 6 May 2021
Accepted: 14 June 2021
Published: 1 July 2021

1. Introduction

Over the last two decades, the synthesis of self-assembled tin oxide (SnO_2) semiconductor nanoparticles has been a fascinating research area because of their potential applications in gas sensing, lithium-ion batteries, solar cells, and catalysts for various organic reactions [1]. These versatile applications associated with their photophysical, chemical, and electronic properties can be realized by tuning certain factors, such as the size, shape, crystallinity, and electronic states of the SnO_2 nanoparticles [2]. In particular, self-assembled 3D SnO_2 nanoaggregates with high surface areas [3,4] have received considerable attention. A bottom-up, wet-chemical synthesis is one of the major techniques that enables the creation of nanoparticles with various dimensions, ranging from spherical morphologies [5] to anisotropic 1D structures [6], 2D sheets [7], and self-assembled 3D forms [1] of low-dimensional motifs. Thus far, such SnO_2 production has relied heavily on hydrothermal synthesis, which requires a high temperature and pressure. As an example, to form the target hierarchical nanostructures, a conventional hydrothermal approach has

been reported to produce a 3D flower-like SnO_2 nano/microstructure material [8]. From the $SnCl_4$ precursor solution with a poly (acrylic acid) additive, flower-like particles with a dimension of 100 nm consisting of needle-like single-crystal units (ca. 50 nm in size) were obtained under acidic conditions at 150 °C. Several other syntheses of SnO_2 particles with flower-like morphology have also been reported to date, using various Sn (II) precursors under hydrothermal conditions [9,10].

A low-temperature solution process employing a sol-gel method is considered an alternative method for creating oxide nanoparticles with high surface areas. This is because, in this method, nucleation and crystal growth at a single nanometer scale can be controlled by the selection of base solvents, metal-ion sources, and organic additives, compared to the cases in the well-known hydrothermal or solvothermal methods. Among wide-bandgap semiconductor metal oxides, several controlled low-temperature hydrolyses and polycondensations in TiO_2 syntheses have been shown to produce TiO_2 nanoparticles of different sizes, crystal phases, and morphologies, with dimensions of less than 10 nm [11,12]. We recently demonstrated that organic-inorganic Ti (IV)-gels prepared at temperatures as low as 40 °C could be used as a precursor to obtain anatase TiO_2 nanoaggregates consisting of particles with a grain size of 5 nm [13]. Freeze drying of the gel precursor accelerates the polycondensation in the Ti-O framework to efficiently produce nanocrystals even at low temperatures.

In contrast to the several low-temperature TiO_2 syntheses reported in the literature, the growth mechanism of SnO_2 nanoparticles and their 3D structure formation at low temperatures have not been adequately understood to date. SnO_2 films processed at relatively low temperatures are regarded as attractive materials with the progress of new-generation solar cells, specifically halide perovskite solar cells [14–18]. Therefore, fundamental research regarding SnO_2 crystallization is essential for developing electron-transport materials that boost device performance.

In this study, simple template-free reaction conditions employing $SnCl_2$ and Na_2CO_3 in water were applied to investigate a low-temperature SnO_2 crystal growth, along with freeze-drying. The formation of 3D SnO_2 nanoaggregates with uniform, single nanometer-scale grains, and their crystallization were clarified, mainly using reaction time-dependent, high-resolution HRTEM analysis. For the first time, we showed the low-temperature crystal growth characteristics of SnO_2 nanoaggregates involving the formation of oxygen vacancies. The detailed crystallization of the pre-organized Sn-based gel precursors was assessed to form 3D SnO_2 nanoaggregates with controllable microstructure surfaces and electronic properties.

2. Materials and Methods

2.1. Synthesis of SnO_2 Nanoaggregates

$SnCl_2{\cdot}2H_2O$ and Na_2CO_3 were purchased from Sigma-Aldrich, St. Luis, Missouri, USA and used as received. Three different synthesis methods were applied to synthesize the semiconductor SnO_2 nanoparticles. The mass ratio of ultrapure water (UPW), $SnCl_2$, and Na_2CO_3 were varied, as shown in Methods 1–3 below.

Method 1: The precursor solution was prepared by mixing $SnCl_2$ (2 g) dissolved in UPW (400 mL). Na_2CO_3 (400 mg) was dissolved separately in UPW (500 mL) and completely mixed with the $SnCl_2$ solution. The solution was placed in a water bath and maintained at 40 °C for a given time, denoted as Day X (X: 1–7 or 1–8) hereinafter. The SnO_2 solution was sampled by transferring 150 mL to a centrifugation container. Thereafter, the container was centrifuged at 4000 rpm for 10 min. The reaction temperature was maintained at 40 °C. After centrifugation, the liquid was discarded. The solid gel was carefully mixed in 5–10 mL of water and sonicated for uniform dispersion. Subsequently, it was added to a vial and capped. The vial was placed in a container filled with liquid nitrogen for 5–10 min to freeze the gel solution. Afterward, the vial was placed into a jar and attached to a vacuum freeze-drying apparatus (BenchTop Pro with Omnitronics, VirTis

SP Scientific, USA) at ~200 mTorr. After 24–48 h of freeze-drying to remove the moisture, SnO_2 nanoparticles were produced in a powdered form.

Method 2: The precursor solution was prepared using a mixture of $SnCl_2$ (5 g) dissolved in UPW (500 mL). Na_2CO_3 (500 mg) was dissolved separately in UPW (500 mL) and completely mixed with the $SnCl_2$ solution. Thereafter, the solution was placed in a water bath and maintained at 40 °C for a given period. The SnO_2 nanoparticles were isolated using a similar procedure to that in Method 1.

Method 3: The precursor solution was prepared by dissolving $SnCl_2$ (20 g) in UPW (500 mL), in contrast to using 5 g of $SnCl_2$, as in Method 2. The SnO_2 nanoparticles were isolated using a similar procedure to that in Method 1.

2.2. Structure Characterization of SnO_2 Nanoaggregates

SnO_2 powder samples were characterized using X-ray diffraction (XRD; Rigaku RINT Ultima/PC with monochromated Cu–Kα radiation, Tokyo, Japan). The crystallite size of the SnO_2 aggregates was estimated using the Scherrer equation ($D = K\lambda/\beta\cos\theta$) based on the XRD data, where D, K, λ, and θ indicate the crystallite size, Scherrer constant (0.90), X-ray wavelength (1.54 Å), and Bragg angle, respectively. The SnO_2 sample surface was analyzed by XPS (XPS; ULVAC, Quantera SXM, Kanagawa, Japan). Nanostructure analysis was carried out by TEM (JEM-2100, Tokyo, Japan). The Brunauer–Emmett–Teller (BET) surface area was evaluated by N_2 physisorption measurement at 77 K, using the Micromeritics TriStar II 3020 (Kyoto, Japan). Photoabsorption spectra were measured using a Hitachi U-4000 spectrophotometer. Ultraviolet–visible (UV–Vis) spectra were obtained from the diffuse reflectance of the dry powder samples.

3. Results

3.1. XRD Patterns and XPS Spectra of the Obtained Powder Samples

We previously reported that anatase TiO_2 nanoaggregates can be produced by freeze drying using Ti-gel precursors [13]. This result stimulated our interest in the growth control of SnO_2 nanoaggregates at low temperatures. The XRD patterns of the powder samples obtained using three sets of reactions (Methods 1–3) are shown in Figure 1a–c. All the observed peaks are in agreement with those of tetragonal rutile SnO_2 (JCPDS 01-072-1147), except for the Method 1–Day 1 sample. In the early stage of the sol–gel process in Method 1, only the impurity phase of NaCl is detected, and no SnO_2 peak is observed. All the peaks corresponding to SnO_2 are identified for the rest of the samples obtained via Method 1. It is observed that the intensity of the SnO_2 peaks increases with the reaction times for all methods, indicating that long reaction times lead to the enhancement of the SnO_2 crystal growth.

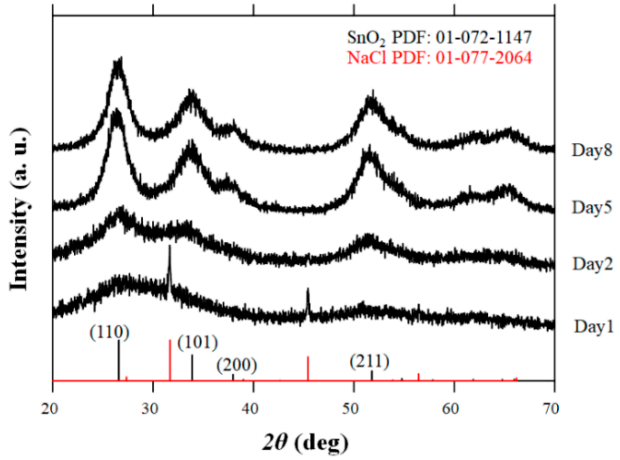

(**a**) XRD pattern of SnO_2 samples synthesized using Method 1. For Day 1 sample, no SnO_2 peak was observed.

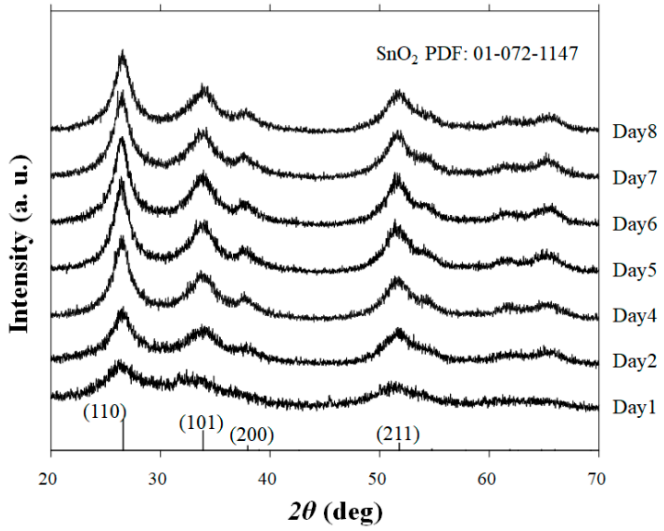

(**b**) XRD pattern of SnO_2 samples synthesized using Method 2.

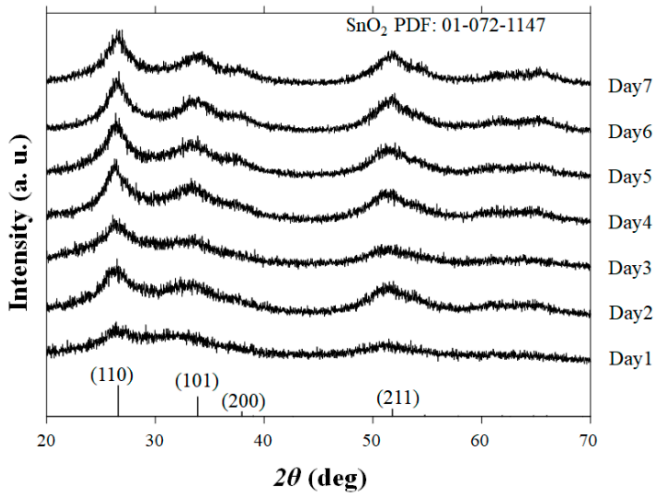

(**c**) XRD pattern of SnO_2 samples synthesized using Method 3.

Figure 1. Powder X-ray diffraction (XRD) patterns of Method 1–3 samples synthesized by varying the reaction times. The database pattern is presented at the bottom of each figure.

The samples obtained via Methods 1 and 2 exhibited a pale-yellow color when the solgel reactions were stopped in a short time (except for the Method 1–Day 1 samples, which exhibited a white color), and became white when the reactions were extended. Conversely, all the samples for Method 3 had a pale-yellow color (Figure 2). To understand the color-change tendency, XPS measurements of Method 1–Day 1, Method 1–Day 8, Method 2–Day 8, and Method 3–Day 7 samples were carried out as illustrated in Figure 3a,b. The binding energies corresponding to the peaks of Sn 3d5/2 for the Day 7 and 8 samples were 486.2, 486.4, and 486.2 eV for Method 3–Day 7, Method 1–Day 8, and Method 2–Day 8, respectively, which are almost consistent with the reported values for Sn(IV) bound to an oxygen atom in SnO_2 [19–21]. Notably, all three pale-yellow samples showed a marked peak shift compared to that of the Method 1–Day 1 sample. For the Method 1–Day 1 sample, the Sn3d XPS peaks were observed at a lower binding energy (485.2 eV) than those for the other samples, suggesting that the Sn(II) in this sample was not oxidized to Sn(IV). Similarly, a peak shift was observed for the pale-yellow sample (Method 2–Day 1) when compared to that of Method 1–Day 1, as shown in Figure 3c.

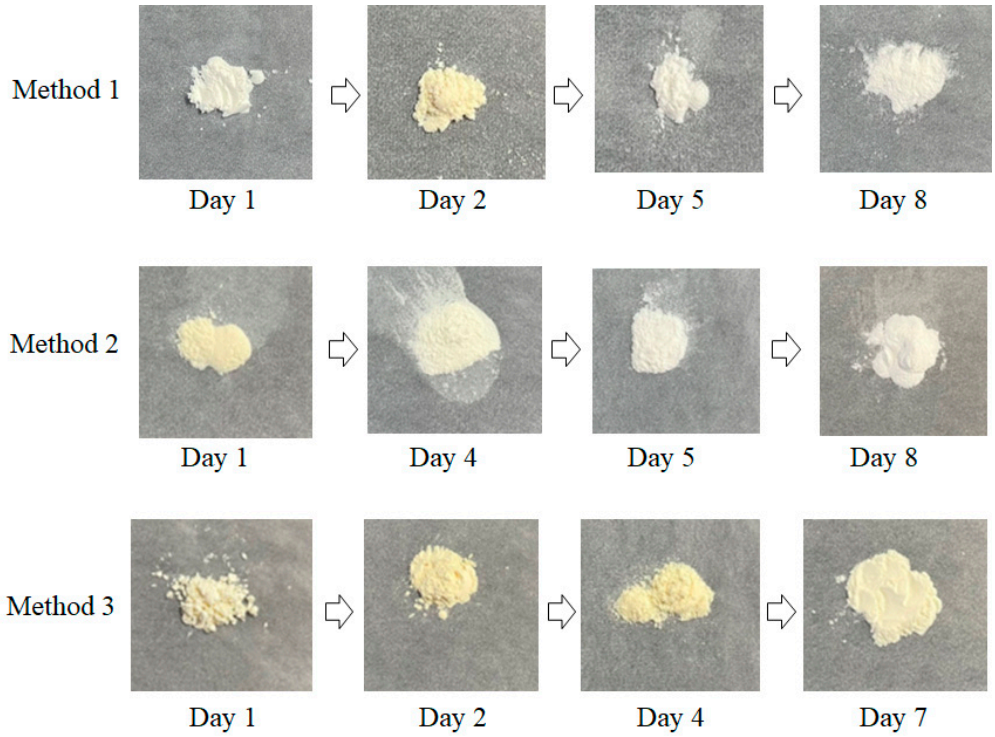

Figure 2. Photographs of the obtained representative powder samples synthesized by a sequential low-temperature sol–gel and freeze-drying approach.

The high-resolution O 1s spectra from the same sample could be deconvoluted into two peaks at approximately 530–532 eV, as indicated by the orange and blue lines. It has been reported that the low energy peak is ascribed to the oxygen bound to Sn atoms, whereas the high energy peak corresponds to the formation of oxygen vacancies [22,23]. Considering that SnO_2 peaks were only detected in the XRD patterns, the large amount of Sn(II) source for Method 3 probably enhanced the formation of oxygen-vacancy-induced SnO_2, even for long reactions.

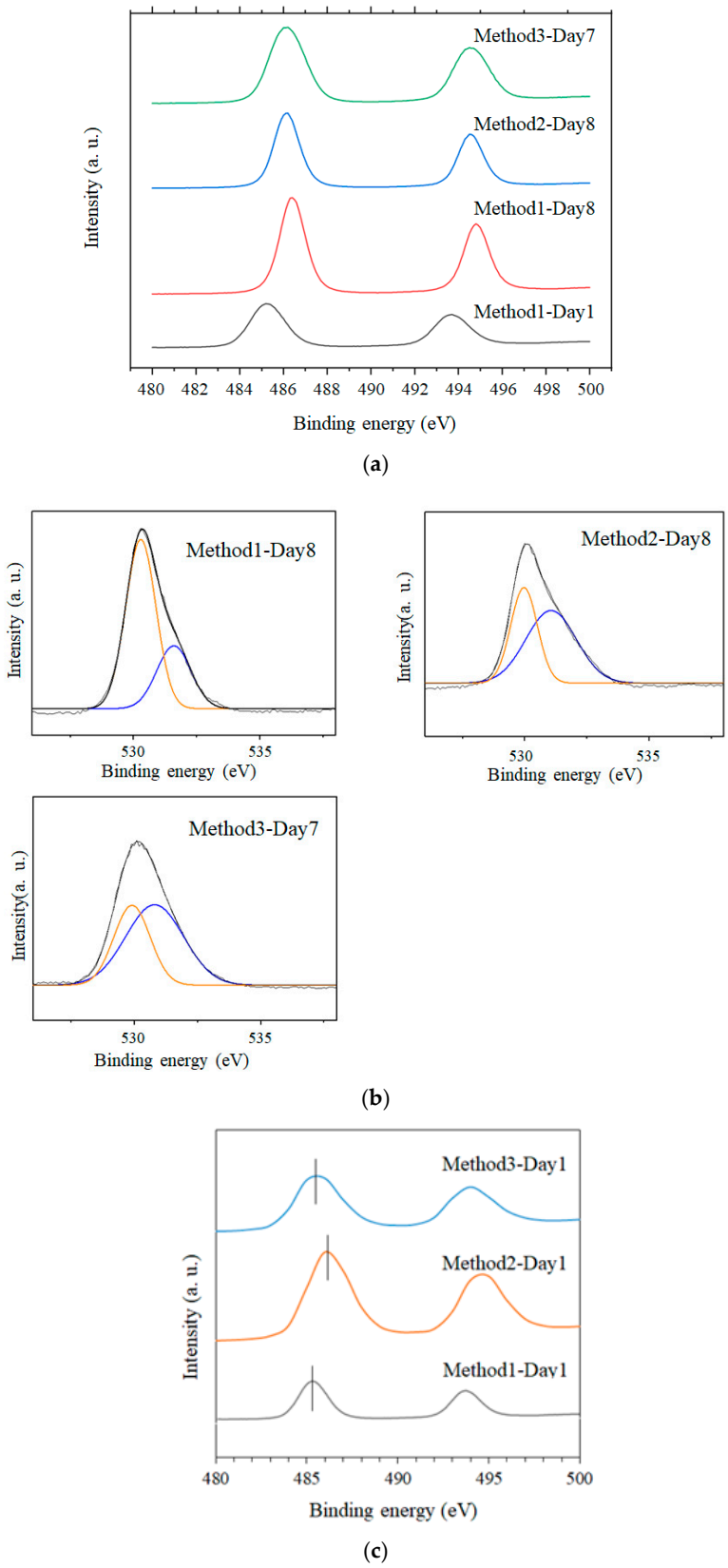

Figure 3. (**a**) X-ray photoelectron spectroscopy (XPS) spectra of Method 1–Day 1, Method 1–Day 8, Method 2–Day 8, and Method 3–Day 7 samples corresponding to Sn 3d5/2; (**b**) XPS spectra of the same samples (except Method 1–Day 1) showing O 1s peaks; (**c**) XPS spectra of Method 3–Day 1, Method 2–Day 1, and Method 1–Day 1 samples.

3.2. Proposed Growth Mechanism of SnO_2 Based on TEM Analysis and Its Optical Property

To resolve the SnO_2 nanostructures and elucidate their growth mechanism, HRTEM measurements were performed, as shown in Figure 4. The crystallization was not significant for all early-stage samples, such as the Method 1–Day 1 sample, as shown in the selected area diffraction (SAD) pattern (not shown). As the reaction times increase, lattice fringes with d-spacings of 0.33 nm and 0.27 nm corresponding to the (110) and (101) planes, respectively, are clearly observed for all methods. The measurements indicated that the aggregated particles consisting of tiny nanocrystals were formed from precursor Sn(II)-based gels, where the average sizes of the primary nanocrystals were in the range of 2~5 nm (Table 1), which are consistent with the estimated crystallite sizes in Table 2. Notably, the diffraction spots in SAD patterns become more noticeable as the reaction proceeds, although the corresponding measured area showed numerous tiny nanoparticles, as shown in Figure 5. This further indicated the improved crystallinity of the long-reaction-time samples.

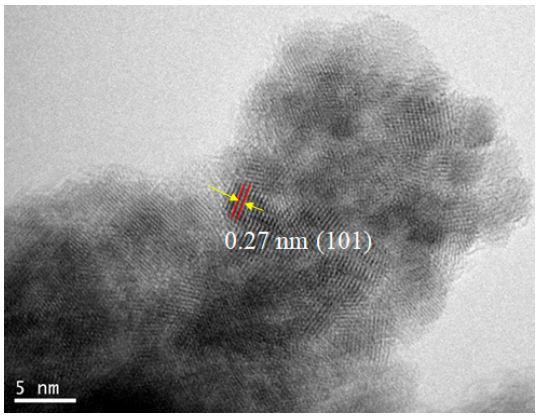

(**a**)

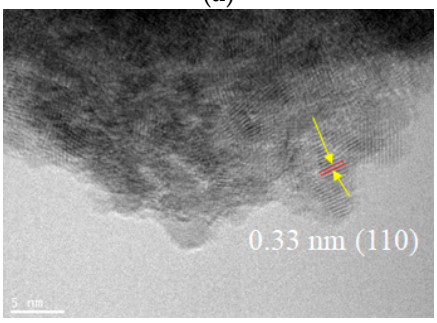

(**b**)

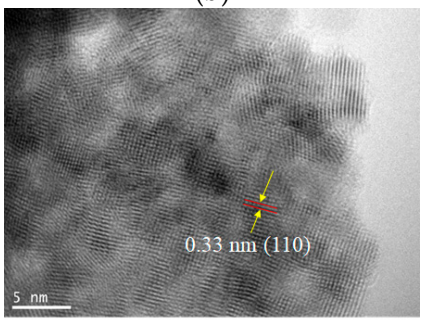

(**c**)

Figure 4. *Cont.*

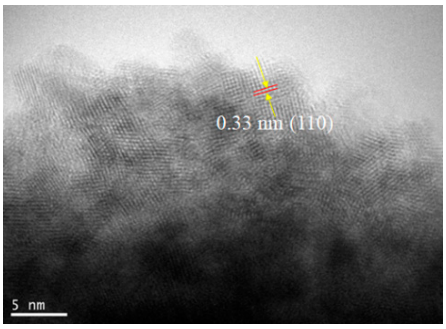

(**d**)

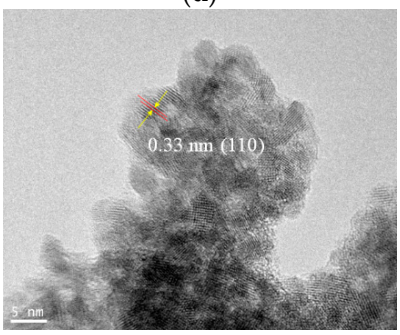

(**e**)

Figure 4. Transmission electron microscopy (TEM) images of (**a**) Method 1–Day 5, (**b**) Method 2–Day 1, (**c**) Method 2–Day 5, (**d**) Method 3–Day 1, and (**e**) Method 3–Day 5 samples.

Table 1. Sizes of SnO_2 particles in the nanoaggregates observed in the TEM images of Figure 4a–e. The maximum length perpendicular to the lattice fringes of SnO_2 nanoparticles was measured. The average nanoparticle sizes for the TEM images (**a**)–(**e**) were 2.6 nm, 2.7 nm, 4.4 nm, 3.5 nm, and 4.3 nm, respectively.

Nanoparticles	Size of Nanoparticles (nm)				
	Method 1-Day 5	Method 2-Day 1	Method 2-Day 5	Method 3-Day 1	Method 3-Day 5
1	2.7	2.4	5.0	4.3	4.3
2	2.8	2.6	3.9	3.4	4.2
3	2.0	2.9	4.9	2.6	4.2
4	2.0	2.7	4.3	3.6	4.6
5	3.0		4.0	3.4	4.4
6	3.0		4.4		4.7

Table 2. Crystallite sizes and specific surface areas of the SnO_2 samples synthesized using different reaction conditions and times.

Methods and Days	Crystalline Size (mm)	Specific Surface Area (m^2/g)
M1D2	2	44
M1D5	3	112
M2D1	3	44
M2D2	3	152
M2D5	5	133
M3D1	3	5
M3D2	3	52
M3D5	3	65

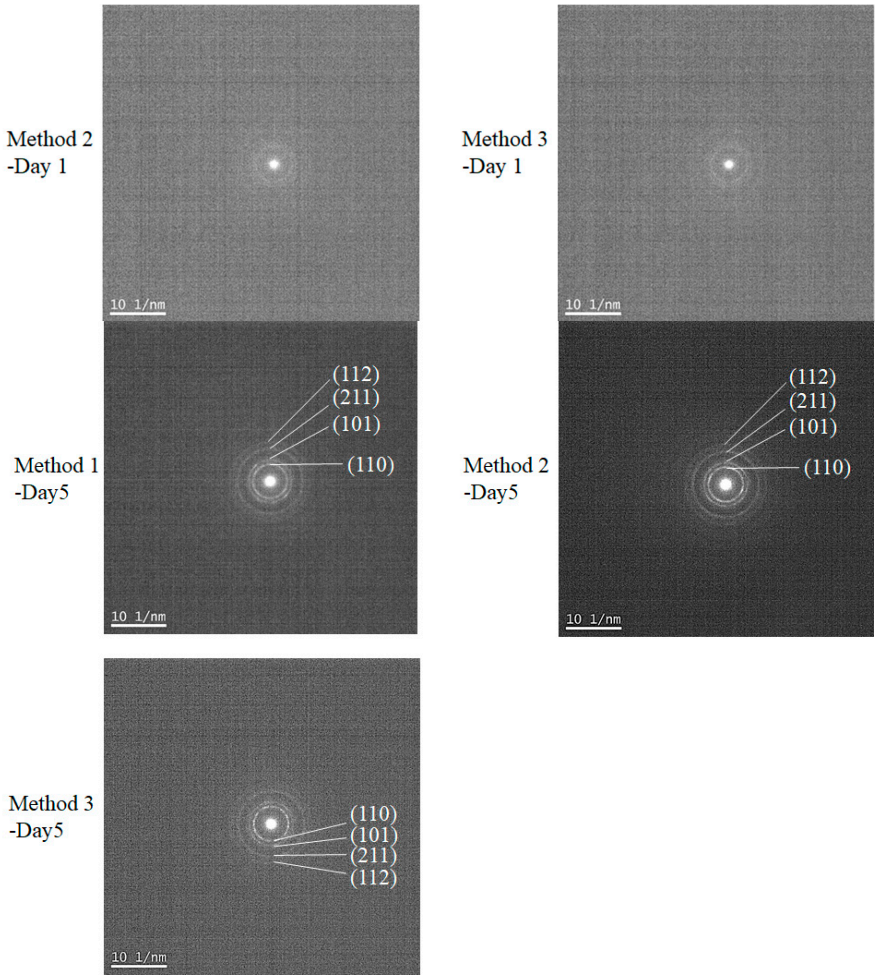

Figure 5. Selected area diffraction (SAD) pattern of Method 1–Day 5, Method 2–Day 1, Method 2–Day 5, Method 3–Day 1, and Method 3–Day 5 samples. These were measured using the same samples as those in Figure 4, which shows the TEM images.

In addition, it was observed that the size of the SnO_2 nanocrystals decreased slightly as the $SnCl_2$ amount increased (Table 2). In our low-temperature process, the amount of $SnCl_2$ was another key factor in controlling the size of the primary SnO_2 nanoparticles, along with their crystallinity and generation rate of oxygen vacancies. As for the growth mechanism of the SnO_2 particles, it is most probable that Sn(II) hydroxide precursors are formed by the hydrolysis of $SnCl_2$ and subsequently converted into submicrometer-scale nanoaggregates comprising uniform SnO_2 spherical nanocrystals. Figure 6 shows a conceptual drawing of the crystal growth characteristics of the SnO_2 nanoaggregates in our low-temperature sol–gel reaction of Sn(II) and the subsequent freeze-drying process. The longer the sol–gel reaction time, the more enhanced the crystallization through its neighboring particles in a confined part of the nanoaggregates, while the specific surface areas of the SnO_2 samples increase. In other words, long reactions produce SnO_2 nanoaggregates with single-nanometer-scale lumpy surfaces, providing increased specific surface areas.

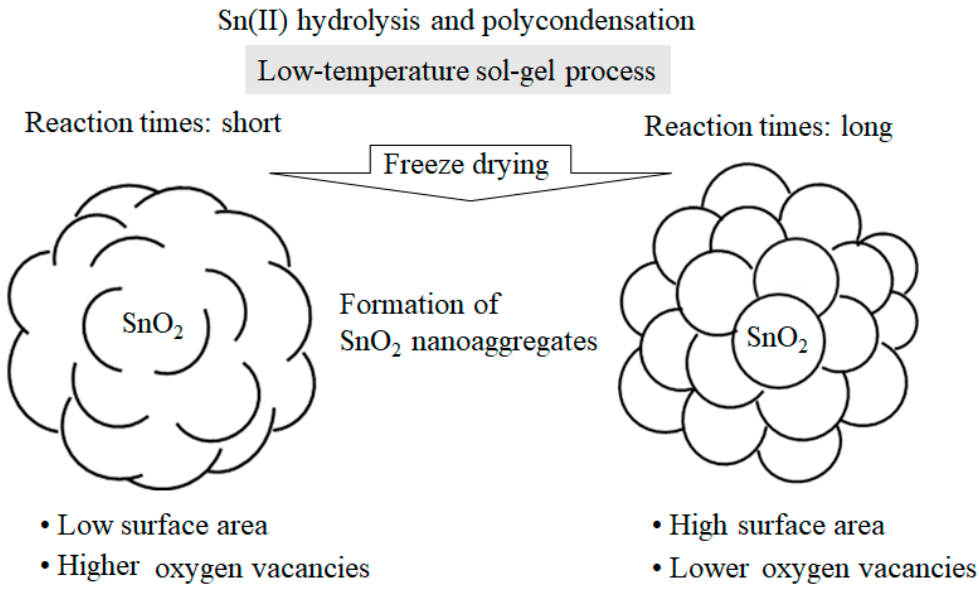

Figure 6. Plausible crystal growth mechanism of SnO_2 nanoaggregates depending on reaction times of the low-temperature sol–gel process.

For Methods 2 and 3, the specific surface areas for Days 2 and 5 were almost comparable, suggesting that both SnO_2 nanoaggregates for Day 2 already had lumpy surfaces, as illustrated on the right in Figure 6. Therefore, it is most likely that the SnO_2 nanoaggregates after 3–4 days had surfaces similar to the image on the right. For Method 1, it would also be reasonable that, with increasing the reaction times, the SnO_2 surface morphology changes from left to right, as shown in Figure 6. However, the surface morphology after 3–4 days cannot be explained solely by the change of the specific surface areas between Day 2 and Day 5. More detailed nanostructure analyses of the assembled SnO_2 particles, i.e., 3D grain growth, will benefit from theoretical/computational modeling, in combination with the HRTEM data of SnO_2 particles [24].

Additionally, we measured the optical absorption of several SnO_2 samples of Methods 1–3 using diffuse reflectance spectroscopy, as shown in Figure 7. Notably, the samples of Method 1–Day 2, Method 2–Day 2, Method 3–Day 2, and Method 3–Day 7 showed an absorption tail in the visible wavelength. Their observed bandgaps were estimated to be 3.1, 3.0, 2.9, and 3.1 eV for Method 1–Day 2, Method 2–Day 2, Method 3–Day 2, and Method 3–Day 7, respectively. It was reported that the narrower bandgaps compared to a well-known bandgap of 3.6 eV [2,25] is due to the elevation of the valence-band maximum of SnO_2 induced by the oxygen vacancies [22,26]. The bandgap of Method 1–Day 8 and Method 2–Day 7 was 3.6 eV.

As has been demonstrated in solar cells, such as perovskite solar cells, sintering SnO_2 nanoparticles can enhance electron transport properties [14]. Additional studies to evaluate the sintering effects of the obtained SnO_2 particles on solar cell performance are in progress.

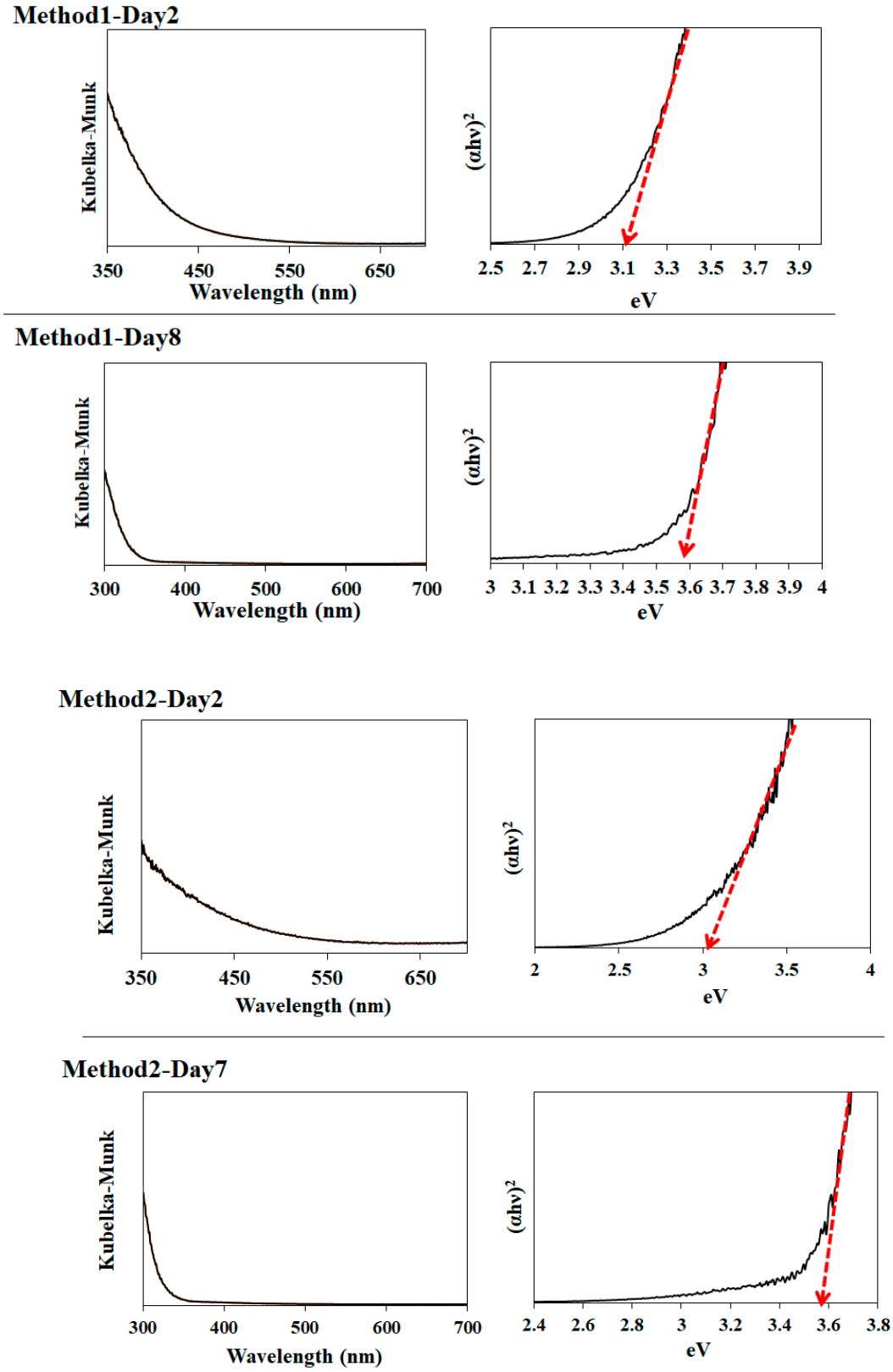

Figure 7. *Cont.*

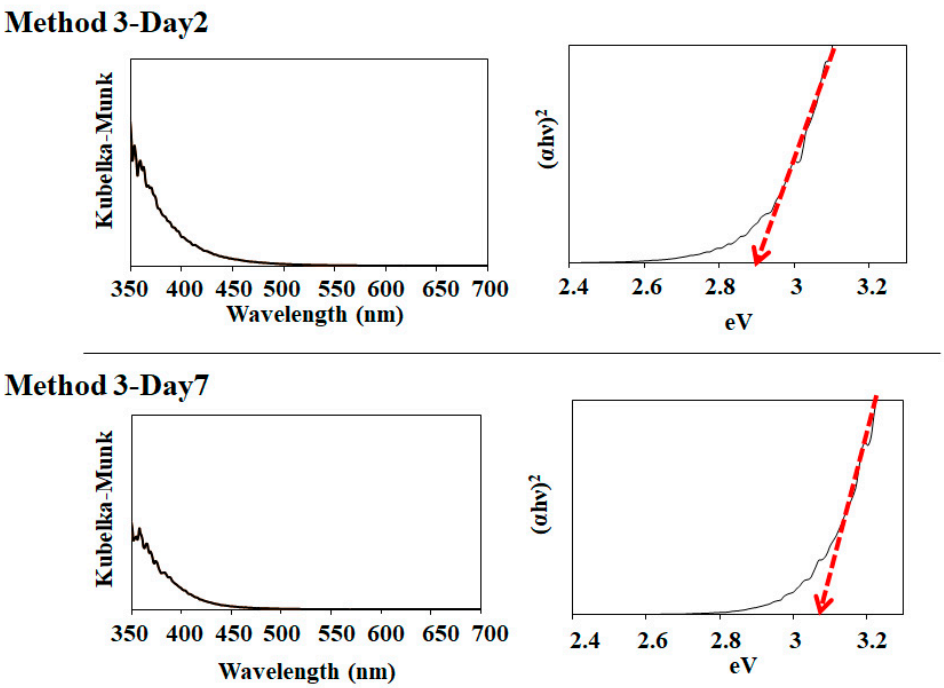

Figure 7. Photoabsorption spectra of Method 1–Day 2, Method 1–Day 8, Method 2–Day 2, Method 2–Day 7, Method 3–Day 2, Method 3–Day 7 samples and their corresponding bandgap estimations.

4. Conclusions

A low-temperature growth mechanism of SnO_2 nanoaggregates has been presented for the first time, based on HRTEM, XRD, and XPS analyses of a series of SnO_2 samples. The changes in the $SnCl_2$ and Na_2CO_3 concentrations in the reaction mixture enabled the control of the lumpy surface of SnO_2 at the single-nanometer scale, as well as the Sn (II) formation in the SnO_2 aggregates. As the sol-gel reaction times increased, the TEM data suggested that the crystallization of tiny nanoparticles was enhanced to form SnO_2 nanoaggregates with high specific surface areas. In addition, oxygen-vacancy-induced SnO_2 nanoaggregates could be obtained by adjusting certain factors, including the reaction time and starting material concentrations of $SnCl_2$ and Na_2CO_3. Such a low-temperature synthesis of 3D SnO_2 will provide new avenues for developing and producing high-performance functional nanomaterials cost-effectively. Our findings will provide insights for the further investigation of 3D SnO_2 and its related functions for versatile applications.

Author Contributions: Conceptualization, S.V. and K.M.; methodology, S.V. and K.M.; formal analysis, N.H., K.M. and T.S.; synthesis, S.V., K.M., A.W., C.E. and U.S. writing—original draft preparation, S.V. and K.M.; writing—review and editing, S.V., K.M., A.W.; project administration, S.V.; funding acquisition, S.V. and K.M. All authors have read and agreed to the published version of the manuscript.

Funding: This work was supported by the Illinois Space Grant Consortium, USA, the Research Excellence Program and the Caterpillar Fellowship, Bradley University, USA. This work is also supported by the OGAWA Science and Technology Foundation, Japan.

Conflicts of Interest: The authors declare no conflict of interest.

References

1. Wang, H.; Rogach, A.-L. Hierarchical SnO_2 nanostructures: Recent advances in design, synthesis, and applications. *Chem. Mater.* **2014**, *26*, 123–133. [CrossRef]
2. Periyasamy, M.; Kar, A. Modulating the properties of SnO_2 nanocrystals: Morphological effects on structural, photoluminescence, photocatalytic, electrochemical and gas sensing properties. *J. Mater. Chem. C.* **2020**, *8*, 4604–4635. [CrossRef]

3. Wang, B.-J.; Ma, S.-Y.; Pei, S.-T.; Xu, X.-L.; Cao, P.-F.; Zhang, J.-L.; Zhang, R.; Xu, X.-H.; Han, T. High specific surface area SnO_2 prepared by calcining Sn-MOFs and their formaldehyde-sensing characteristics. *Sens. Actuators B Chem.* **2020**, *321*, 128560. [CrossRef]
4. Zhao, Q.; Ma, L.; Zhang, Q.; Wang, C.; Xu, X. SnO_2-Based Nanomaterials: Synthesis and Application in Lithium-Ion Batteries and Supercapacitors. *J. Nanomater.* **2015**, 850147. [CrossRef]
5. Kim, H.; Kim, M.-C.; Kim, S.-B.; Kim, Y.-S.; Choi, J.-H.; Park, K.-W. Porous SnO_2 nanostructure with a high specific surface area for improved electrochemical performance. *RSC Adv.* **2020**, *10*, 10519–10525. [CrossRef]
6. Matysiak, W.; Tański, T.; Smok, W.; Polishchuk, O. Synthesis of hybrid amorphous/crystalline SnO_2 1D nanostructures: Investigation of morphology, structure and optical properties. *Sci. Rep.* **2020**, *10*, 14802. [CrossRef]
7. Wan, W.; Li, Y.; Ren, X.; Zhao, Y.; Gao, F.; Zhao, H. 2D SnO_2 Nanosheets: Synthesis, Characterization, Structures, and Excellent Sensing Performance to Ethylene Glycol. *Nanomaterials* **2018**, *8*, 112. [CrossRef] [PubMed]
8. Uchiyama, H.; Shirai, Y.; Kozuka, H. Hydrothermal synthesis of flower-like SnO_2 particles consisting of single crystalline nano rods through crystal growth in the presence of poly(acrylic acid). *RSC Adv.* **2012**, *2*, 4839–4843. [CrossRef]
9. Lu, Z.; Zhao, Z.; Yang, L.; Wang, S.; Liu, H.; Feng, W.; Zhao, Y.; Feng, F. A simple method for synthesis of highly efficient flower-like SnO_2 photocatalyst nanocomposites. *J. Mater. Sci. Mater. Electron.* **2019**, *30*, 50–55. [CrossRef]
10. Vuong, D.-D.; Hien, V.-X.; Trung, K.-Q.; Chien, N.-D. Synthesis of SnO_2 micro-spheres, nano-rods and nano-flowers via simple hydrothermal route. *Phys. E* **2011**, *44*, 345–349. [CrossRef]
11. Sang, L.; Zhao, Y.; Burda, C. TiO_2 Nanoparticles as Functional Building Blocks. *Chem. Rev.* **2014**, *114*, 9283–9318. [CrossRef]
12. Manseki, K.; Saka, K.; Matsui, M.; Vafaei, S.; Sugiura, T. Structure identification of Ti(iv) clusters in low-temperature TiO_2 crystallization: Creating high-surface area brush-shaped rutile TiO_2. *CrystEngComm* **2017**, *19*, 5844–5848. [CrossRef]
13. Vafaei, S.; Springaire, L.; Schnupf, U.; Hisae, K.; Hasegawa, D.; Sugiura, T.; Manseki, K. Low temperature synthesis of anatase TiO_2 nanocrystals using an organic-inorganic gel precursor. *Powder Technol.* **2020**, *368*, 237–244. [CrossRef]
14. Jena, A.-K.; Kulkarni, A.; Miyasaka, T. Halide perovskite photovoltaics: Background, status, and future prospects. *Chem. Rev.* **2019**, *119*, 3036–3103. [CrossRef] [PubMed]
15. Yoo, J.-J.; Seo, G.; Chua, M.R.; Park, T.-G.; Lu, Y.; Rotermund, F.; Kim, Y.-K.; Moon, C.-S.; Jeon, N.-J.; Correa-Baena, J.-P.; et al. Efficient perovskite solar cells via improved carrier management. *Nature* **2021**, *590*, 587–593. [CrossRef]
16. Yun, A.-J.; Kim, J.; Hwang, T.; Park, B. Origins of Efficient Perovskite Solar Cells with Low-Temperature Processed SnO_2 Electron Transport Layer. *ACS Appl. Energy Mater.* **2019**, *2*, 3554–3560. [CrossRef]
17. Yang, D.; Yang, R.; Wang, K.; Wu, C.; Zhu, X.; Feng, J.; Ren, X.; Fang, G.; Priya, S.; Liu, S.-F. High efficiency planar-type perovskite solar cells with negligible hysteresis using EDTA-complexed SnO_2. *Nat. Commun.* **2018**, *9*, 3239. [CrossRef] [PubMed]
18. Chen, J.-Y.; Chueh, C.-C.; Zhu, Z.; Chen, W.-C.; Jen, A.-K.-Y. Low-temperature electrodeposited crystalline SnO_2 as an efficient electron-transporting layer for conventional perovskite solar cells. *Sol. Energy Mater. Sol. Cells* **2017**, *164*, 47–55. [CrossRef]
19. Sahoo, M.; Ramaprabhu, S. Solar synthesized tin oxide nanoparticles dispersed on graphene wrapped carbon nanotubes as a Li ion battery anode material with improved stability. *RSC Adv.* **2017**, *7*, 13789–13797. [CrossRef]
20. Lin, H.-E.; Katayanagi, Y.; Kishi, T.; Yano, T.; Matsushita, N. A solution-processed tin dioxide film applicable as a transparent and flexible humidity sensor. *RSC Adv.* **2018**, *8*, 30310–30319. [CrossRef]
21. Kwoka, M.; Lyson-Sypien, B.; Comini, E.; Krzywiecki, M.; Waczynski, K.; Szuber, J. Surface properties of SnO_2 nanolayers prepared by spin-coating and thermal oxidation. *Nanotechnology* **2020**, *31*, 315714. [CrossRef] [PubMed]
22. Yang, Y.; Wan, Y.; Yin, S. Oxygen vacancies confined in SnO_2 nanoparticles for desirable electronic structure and enhanced visible light photocatalytic activity. *Appl. Surf. Sci.* **2017**, *420*, 399–406. [CrossRef]
23. Xu, Y.; Zheng, L.; Yang, C.; Liu, X.; Zhang, J. Oxygen Vacancies Enabled Porous SnO_2 Thin Films for Highly Sensitive Detection of Triethylamine at Room Temperature. *ACS Appl. Mater. Interfaces* **2020**, *12*, 20704–20713. [CrossRef]
24. Jamshidian, M.; Thamburaja, P.; Rabczuk, T. A multiscale coupled finite-element and phase-field framework to modeling stressed grain growth in polycrystalline thin films. *J. Comput. Phys.* **2016**, *327*, 779–798. [CrossRef]
25. Entradas, T.; Cabrita, J.-F.; Dalui, S.; Nunes, M.-R.; Monteiro, O.-C.; Silvestre, A.-J. Synthesis of sub-5 nm Co-doped SnO_2 nanoparticles and their structural, microstructural, optical and photocatalytic properties. *Mater. Chem. Phys.* **2014**, *147*, 563–571. [CrossRef]
26. Kamble, V.-B.; Umarji, A.-M. Defect induced optical bandgap narrowing in undoped SnO_2 nanocrystals. *AIP Adv.* **2013**, *3*, 082120. [CrossRef]